

ARTICLE

Open Access

# Advancing on-chip Kerr optical parametric oscillation towards coherent applications covering the green gap

Yi Sun<sup>1,2</sup>, Jordan Stone<sup>1,2</sup>, Xiyuan Lu<sup>1,2</sup>, Feng Zhou<sup>1,2</sup>, Junyeob Song<sup>1</sup>, Zhimin Shi<sup>3</sup> and Kartik Srinivasan<sup>1,2</sup>

## Abstract

Optical parametric oscillation (OPO) in Kerr microresonators can efficiently transfer near-infrared laser light into the visible spectrum. To date, however, chromatic dispersion has mostly limited output wavelengths to  $>560$  nm, and robust access to the whole green light spectrum has not been demonstrated. In fact, wavelengths between 532 nm and 633 nm, commonly referred to as the “green gap”, are especially challenging to produce with conventional laser gain. Hence, there is motivation to extend the Kerr OPO wavelength range and develop reliable device designs. Here, we experimentally show how to robustly access the entire green gap with Kerr OPO in silicon nitride microrings pumped near 780 nm. Our microring geometries are optimized for green-gap emission; in particular, we introduce a dispersion engineering technique, based on partially undercutting the microring, which not only expands wavelength access but also proves robust to variations in resonator dimensions. Using just four devices, we generate  $>150$  wavelengths evenly distributed throughout the green gap, as predicted by our dispersion simulations. Moreover, we establish the usefulness of Kerr OPO to coherent applications by demonstrating continuous frequency tuning ( $>50$  GHz) and narrow optical linewidths ( $<1$  MHz). Our work represents an important step in the quest to bring nonlinear nanophotonics and its advantages to the visible spectrum.

## Introduction

The development of compact visible lasers will benefit numerous sectors of science and industry, including laser lighting and displays<sup>1,2</sup>, spectroscopy for timekeeping and sensing<sup>3–5</sup>, medical practices<sup>6</sup>, and quantum technology<sup>7,8</sup>. While progress has been made in the blue and red wavelength regions, a lack of efficient and compact green laser sources, also known as the “green gap” problem (Fig. 1a), still plagues the laser market<sup>9,10</sup>. III-V semiconductor lasers provide a compelling combination of efficiency and small size<sup>11–14</sup>, but they require Watts of input power and often (especially at “green gap” wavelengths) lack the spectral purity needed for high-

coherence applications<sup>15,16</sup>. Injection locking Fabry-Pérot diode lasers to high-finesse microresonators can improve coherence, but the output wavelengths are constrained by the availability of pump lasers and, so far, are continuously tunable over only a few GHz<sup>17</sup>. In Fig. 1a, we compare various commercial solutions to the green gap problem<sup>18–20</sup>, charting them by their size and wavelength range.

Another way to produce green laser light is through nonlinear optical processes. This is the strategy adopted most by industry, and it offers an intriguing path to scalability via photonic integration since small optical volumes promote efficient nonlinear interactions (commercial instruments using bulk optical components are typically  $\approx 1$  m<sup>3</sup> in size). For example, nonlinear microresonators can generate the frequency harmonics of near-infrared pump lasers to produce visible light, albeit with limited wavelength tuning capability<sup>21–27</sup>. Alternatively, widely-separated Kerr optical parametric oscillation (OPO) is a flexible approach to generate visible light by

Correspondence: Xiyuan Lu (xnl9@umd.edu) or Kartik Srinivasan (kartik.srinivasan@nist.gov)


<sup>1</sup>Microsystems and Nanotechnology Division, Physical Measurement Laboratory, National Institute of Standards and Technology, Gaithersburg, MD, USA

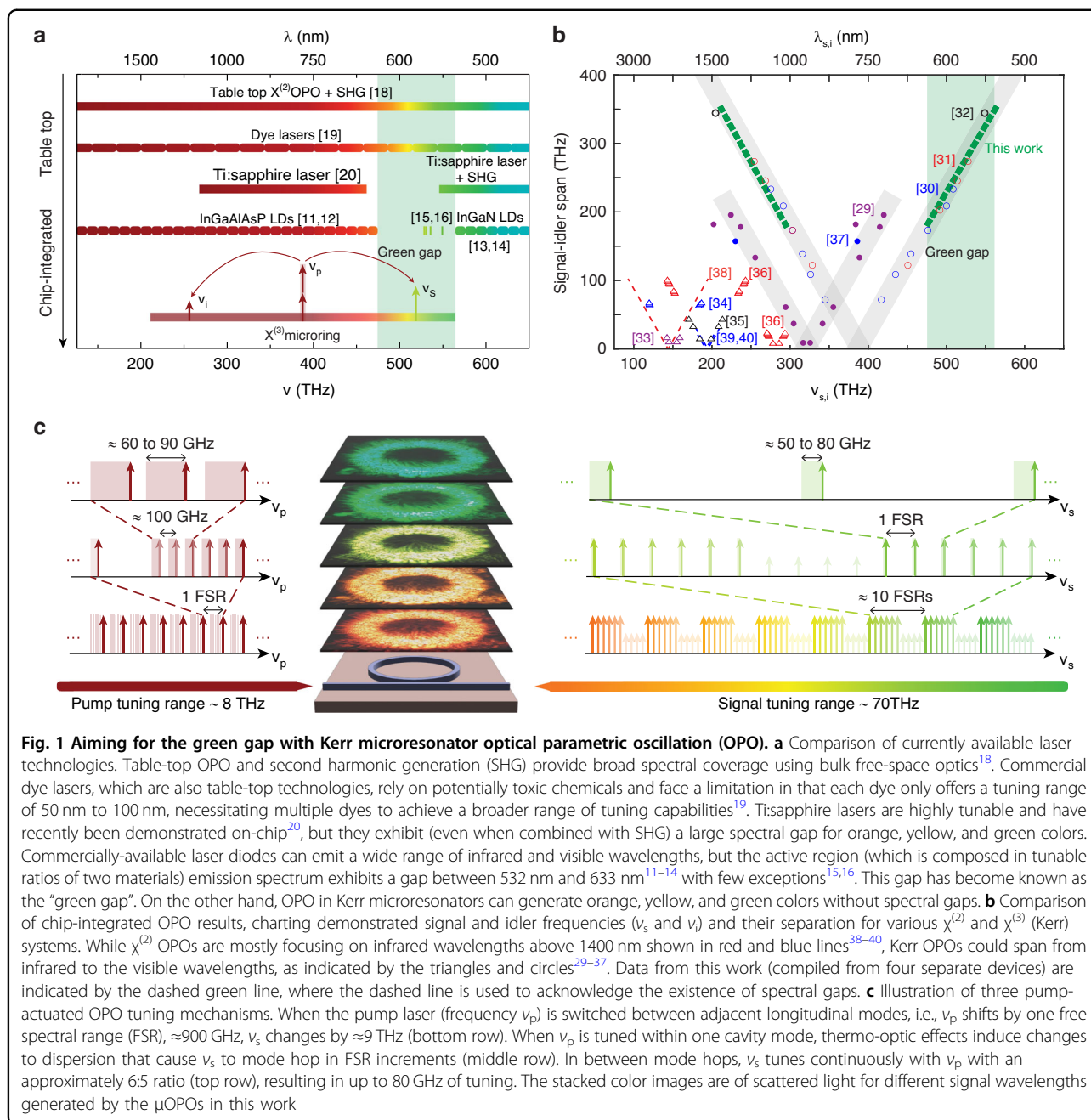
<sup>2</sup>Joint Quantum Institute, NIST/University of Maryland, College Park, MD, USA

Full list of author information is available at the end of the article

These authors contributed equally: Yi Sun, Jordan Stone

© This is a U.S. Government work and not under copyright protection in the US; foreign copyright protection may apply 2024

 **Open Access** This article is licensed under a Creative Commons Attribution 4.0 International License, which permits use, sharing, adaptation, distribution and reproduction in any medium or format, as long as you give appropriate credit to the original author(s) and the source, provide a link to the Creative Commons licence, and indicate if changes were made. The images or other third party material in this article are included in the article's Creative Commons licence, unless indicated otherwise in a credit line to the material. If material is not included in the article's Creative Commons licence and your intended use is not permitted by statutory regulation or exceeds the permitted use, you will need to obtain permission directly from the copyright holder. To view a copy of this licence, visit <http://creativecommons.org/licenses/by/4.0/>.



four-wave mixing (FWM) from, e.g., a near-infrared pump, and in recent years, OPO based on FWM in optical microresonators (we dub such devices “ $\mu$ OPOs”) has been investigated<sup>28–37</sup>. In these systems, energy from a monochromatic pump laser with frequency  $\nu_p$  is transferred to a blue-shifted signal wave ( $\nu_s$ ) and red-shifted idler wave ( $\nu_i$ ), as shown in Fig. 1a. Visible  $\mu$ OPOs can operate with milliwatt-level threshold powers and have shown pump-to-sideband conversion efficiencies up to 15%<sup>29,30</sup>. In Fig. 1b, we compare the operating wavelengths and spectral separations,  $\nu_s - \nu_i$ , reported in several

$\mu$ OPO studies, including, for completeness, several demonstrations of OPO in  $\chi^{(2)}$  nanophotonics<sup>38–40</sup>. Importantly, signal frequencies in the green spectrum have been reported<sup>30–32</sup>, but the highest frequency reported so far is  $\approx 548.9$  THz<sup>32</sup>, which is  $\approx 14.6$  THz shy from the edge of the green gap. In addition, the  $\mu$ OPO output power and wavelength are sensitive to external parameters like temperature, pump power, and pump-resonator detuning<sup>41</sup>, as well as to microring geometry. These sensitivities tend to grow in proportion to the  $\mu$ OPO separation ( $\nu_s - \nu_i$ ) [ref. 31] and therefore present a

major challenge for  $\mu$ OPOs aiming at more comprehensive coverage of the green gap.

Here, we use  $\mu$ OPOs to access the entire green gap, achieving the highest frequency of  $\approx 563.51$  THz, increasing wavelength access by  $\approx 14.2$  nm beyond the previous record in ref. <sup>32</sup> and improving robustness with respect to parameter variations. Using just four devices, we can selectively generate  $>150$   $\mu$ OPOs, each with a unique green-gap signal frequency that is separated from its nearest neighbor by roughly the microresonator free spectral range (FSR). This breakthrough is enabled by a novel dispersion design in which the substrate is partially etched away, so that a greater portion of the microresonator is air-clad. We perform simulations and measurements to explore the effects of such an undercut on the  $\mu$ OPO. In particular, increasing the undercut makes  $\nu_{s,i}$  less sensitive to  $\nu_p$  and device dimensions; hence, one device supports many green-gap  $\mu$ OPOs, and spectral gaps are filled in using a second device with different dimensions. Our ability to generate a multitude of  $\mu$ OPOs within a single device stems from unique tuning mechanisms (two mode hop-based processes for coarse tuning and one process for continuous fine tuning) that we depict in Fig. 1c. Finally, to prove our  $\mu$ OPOs are well-suited to coherent applications in the green gap, we present measurements of heterodyne beatnotes between the  $\mu$ OPO signal and a separate narrow-linewidth laser, and we characterize the  $\mu$ OPO continuous frequency tunability. We measure fitted linewidths below 1 MHz and continuous tuning ranges up to 80 GHz. With further integration, including recent advancements in chip-integrated 780 nm lasers<sup>17,42,43</sup>,  $\mu$ OPOs are a realistic solution to the green gap problem, especially when low noise is required.

## Results

### Device design

In Fig. 2, we present images of a nominal microring device as well as simulations of the chromatic dispersion. We fabricate microrings out of stoichiometric silicon nitride ( $\text{Si}_3\text{N}_4$ , hereafter written as SiN) with outer ring radius  $RR = 25$   $\mu\text{m}$  and nominal height  $H = 605$  nm; the microrings sit on a  $\text{SiO}_2$  lower cladding and are air-clad on the sides and top (see “Materials and methods” section for details). We couple light in/out of the microrings via two bus waveguides, as shown in Fig. 2a. One waveguide is narrower and runs closer to the microring; it in/out-couples pump and signal light. The other waveguide is wider and farther from the microring and is used to out-couple the long-wavelength idler, which cannot propagate in the narrower waveguide (the waveguide is cut-off at the idler wavelength). Using heated potassium hydroxide, we undercut the microrings by an amount  $U$  that can be between 0 (no undercut) and 1 (completely undercut). In

Fig. 2b, we show a scanning electron microscope image of the microring cross-section in which the undercut ( $U \approx 0.25$ ) is clearly visible.

We choose  $H$  and  $U$  to optimize dispersion, which we parameterize using the frequency mismatch,  $\Delta\nu = \nu_\mu + \nu_{-\mu} - 2\nu_0$ , where  $\nu_\mu$  is the frequency of a mode whose longitudinal mode number (with respect to the pump mode) is  $\mu$ . In general, mode pairs with small positive  $\Delta\nu$  can oscillate<sup>29–31</sup>; hence, to realize  $\mu$ OPOs with wide frequency separations, we desire strong normal group velocity dispersion (GVD) in the pump band (negative curvature of  $\Delta\nu$  around  $\nu_0$ ) and higher-order GVD to balance  $\Delta\nu$  away from  $\nu_0$ . To understand the relationships between  $H$ ,  $U$ , and GVD, in Fig. 2c we present the simulated GVD coefficients,  $\beta_2$  and  $\beta_4$ , for the fundamental transverse electric polarized (TE0) modes of five ring resonators with different ( $H$ ,  $U$ ) values. In the pump band,  $\beta_2$  is slightly positive (indicating normal dispersion) and nearly independent of  $H$  and  $U$ , while  $\beta_4$  becomes significantly more negative for increasing  $H$  and  $U$  (indicating greater higher-order dispersion that can balance the normal dispersion for mode pairs far from the pump). Moreover, we can make the general observation that the idler band (where  $\beta_2$  and  $\beta_4$  are more sensitive to  $\nu$ ,  $H$ , and  $U$ ) primarily determines the geometric dispersion. Alternatively, we can study the  $\Delta\nu$  spectrum and its dependence on  $H$  and  $U$ . In Fig. 2d, e, we present six  $\Delta\nu$  spectra each for devices with (500, 0) and (605, 0.33), respectively, with systematic variations to  $RW$ . In the  $\Delta\nu$  space, zero crossings (marked in Fig. 2d, e by solid circles and squares, respectively) determine  $\nu_s$ , so we can predict specifically the dependence of  $\nu_s$  on  $RW$ ,  $H$ , and  $U$ . In Fig. 2f, we plot  $\nu_s$  versus  $RW$  for several ( $H$ ,  $U$ ) pairs. We find that in the (500, 0) configuration that has been extensively used in prior studies<sup>29–31</sup>,  $\nu_s$  is limited to less than 530 THz, and a relatively narrow range of  $RW$  values allow for green gap emission. However, increasing  $H$  and  $U$  has two notable effects: The maximum realizable  $\nu_s$  is increased, and the  $\mu$ OPO is more robust to geometry perturbations. Specifically, the slope  $d\nu_s/dRW$ , which quantifies the  $\mu$ OPO sensitivity to device dimensions, decreases for increasing  $U$ . As a result, designs are more tolerant to fabrication uncertainties, thus improving device yields when targeting specific wavelengths. In Supplementary Information Fig. S1, we explore the sensitivity of  $\nu_s$  to  $\nu_p$  changes for different geometries and find that it decreases with increasing  $H$  or  $U$ , enabling more  $\mu$ OPOs from individual devices. We also note that, while  $H$  and  $U$  similarly impact the dispersion, thicker waveguides are difficult to etch and are vulnerable to cracking. In the next section, we experimentally verify these concepts and leverage them towards comprehensive access to the green gap.

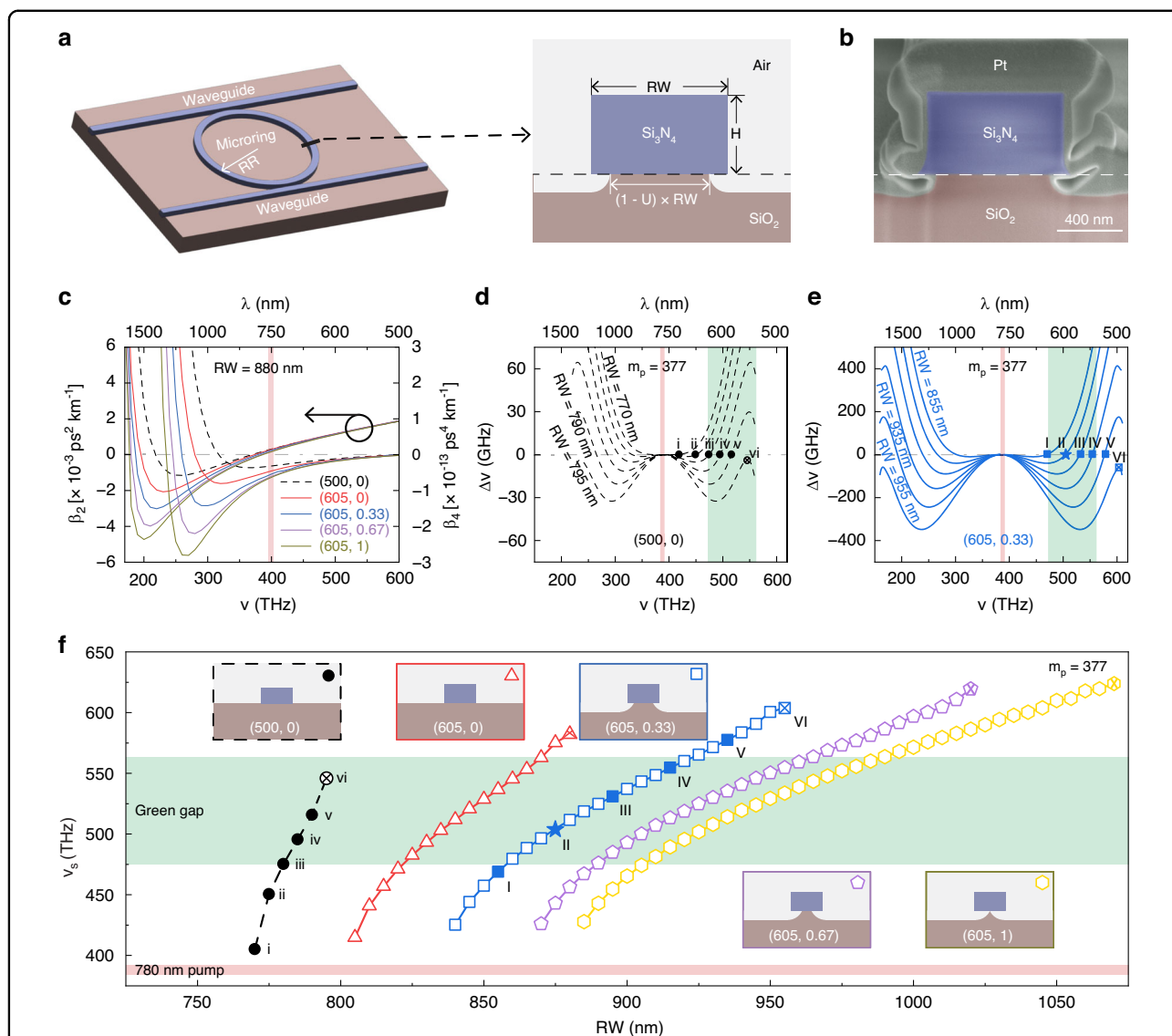


**Fig. 2 Microresonator dispersion design.** **a** Left: Illustration of a microring OPO device, indicating the outer ring radius (RR) and two coupling waveguides that are used for separately extracting the signal and idler waves. Right: Illustration of the microring cross section. The device has a silicon nitride ( $\text{Si}_3\text{N}_4$ , hereafter SiN) core, a silicon dioxide ( $\text{SiO}_2$ ) substrate, and top air cladding. Its dimensions are defined as ring width (RW) and height (H). We also use potassium hydroxide (KOH) to etch the  $\text{SiO}_2$  substrate underneath the SiN core for dispersion engineering. The etch is quantified by the undercut parameter, U. **b** False-color cross-sectional scanning electron microscope (SEM) image from one device milled by focused ion beam. The noticeable "foot" region has a negligible impact on dispersion, as explored through simulations presented in Supplementary Information Fig. S2. **c** Simulations of the second- and fourth-order expansion coefficients ( $\beta_2$  and  $\beta_4$ ) of the TE<sub>0</sub> mode propagation constant for different microring geometries (parameterized as (H, U) and RW = 880 nm). **d** Simulated frequency mismatch spectra for six devices with (500, 0) and RW ranging from 770 nm to 795 nm with increments of 5 nm. Points i-v mark zero crossings, which predict the signal frequency ( $\nu_s$ ). **e** Simulated frequency mismatch spectra for six devices with (605, 0.33) and RW ranging from 855 nm to 955 nm with increments of 20 nm. **f** Simulated values of  $\nu_s$  versus RW for different (H, U) designs. Points marked with numerals correspond to those displayed in **d** and **e**. Data points with crosses mark the upper limit for  $\nu_s$ . For **d-f**, the pump mode azimuthal number,  $m_p$ , is fixed at 377. In general, thicker SiN increases higher-order dispersion to broaden the OPO spectral coverage. We find H = 605 nm is sufficient to cover the green gap. Furthermore, increasing U not only increases spectral coverage but also decreases the sensitivity of  $\nu_s$  to RW, resulting in more robust green light generation and deeper control (e.g., via the tuning mechanisms described in Fig. 1) over the OPO spectrum. Point II, designated with a star symbol, corresponds to our experimental design

### Green gap access

Figure 3 depicts the multitude of green gap  $\mu$ OPOs we make in experiments and illustrates the coarse tuning

mechanisms that enable them. In our experiments, we pump TE<sub>0</sub> modes in a SiN microring with an amplified external cavity diode laser (ECDL) that is continuously

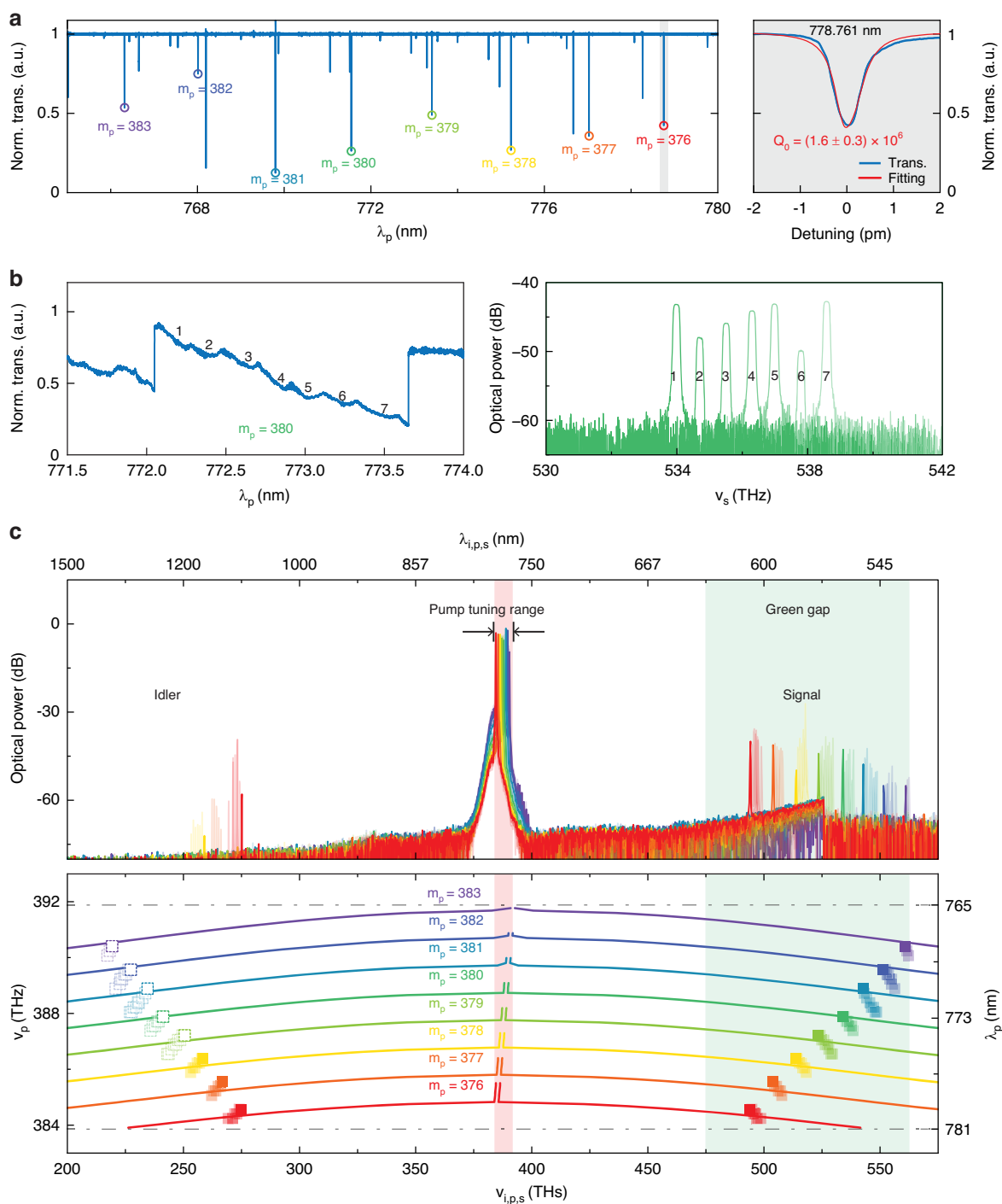


**Fig. 3 Green gap OPO and its coarse tuning.** **a** Normalized pump-band transmission spectrum for a nominal  $\mu$ OPO device with  $H = 605$  nm,  $U = 0.33$ , and  $RW = 875$  nm. Eight TE<sub>0</sub> modes ( $m_p = 376, \dots, 383$ ) are marked with colored circles, and the fitted  $Q$  is shown in the right panel. The quoted uncertainty in  $Q$  is the one standard deviation value from the fit. **b** Left: Normalized high-power transmission for mode  $m_p = 380$  of the device from **a**. We observe the characteristic “thermal triangle” when scanning  $\lambda_p$  from blue to red. Different detunings (marked by numerals 1 through 7) generate seven different  $\mu$ OPOs with  $\nu_s$  differences of approximately one FSR. The corresponding signal spectra are shown in the right panel; here, 0 dB is referenced to 1 mW, i.e., dBm. **c** Top panel: Compilation of optical spectra generated by the nominal device. The different colors correspond to the  $m_p$  values indicated in **a**, and bold data correspond to the first OPO spectrum observed when the pump laser is blue-to-red scanned through a given pump mode. The faded data correspond to subsequently observed OPO spectra (e.g., spectra 2–7 in **b**). Idlers with frequencies below 250 THz are not observed due to the pump/signal access waveguide cutoff (Supplementary Information Fig. S3). Bottom panel: Distribution of the signal and idler frequencies versus simulations. Solid squares are experimental data extracted from the spectra above. Dashed empty squares are estimated based on energy conservation. Solid lines are taken from dispersion simulations



tunable from 765 nm to 781 nm. The measurement setup is illustrated in Supplementary Information Fig. S3. Figure 3a (left panel) depicts the normalized, low-power transmission spectrum of a device with  $RR = 25 \mu\text{m}$ ,  $H = 605 \text{ nm}$ ,  $RW = 875 \text{ nm}$ , and  $U = 0.33$ . The colored circles mark the eight TE<sub>0</sub> modes we can access with the ECDL, and the right panel depicts the normalized transmission zoomed in to 778.761 nm (wavelength measured with a wavemeter with  $\approx 0.1 \text{ pm}$  uncertainty). When we increase the pump power, we can generate OPO, and we observe a characteristic “thermal triangle” shape in the transmission spectrum of each resonator mode when  $\nu_p$  is scanned from blue to red detunings, as shown in the left panel of Fig. 3b. Moreover, for each specific  $m_p$  value (380 in Fig. 3b), adjusting the pump-resonator detuning allows us to tune  $\nu_s$  in FSR-level increments through a mode-switching mechanism<sup>41</sup>, as shown by the seven different signal spectra presented in the right panel of Fig. 3b that correspond to the seven detunings marked in the left panel. The mode switching occurs due to changes in the effective dispersion that arise from Kerr- and thermal-nonlinear mode shifts. Interestingly, we believe that dispersion of the thermo-optic coefficient,  $dn/dT$ , where  $n$  is the refractive index of SiN and  $T$  is the modal temperature, must be considered to properly model the mode switching, but such measurements are not found in the existing literature.

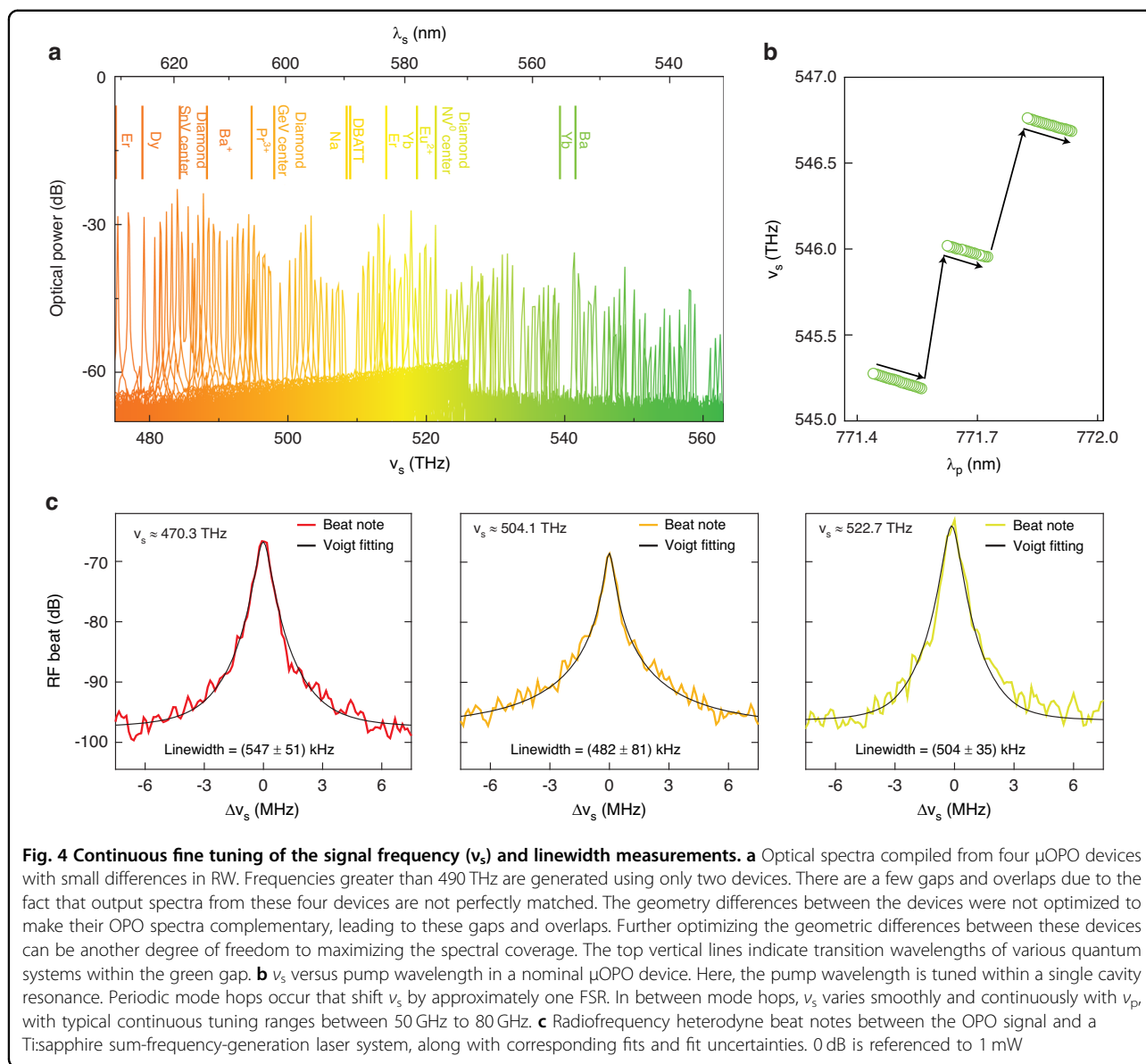
To more widely tune  $\nu_s$ , we can pump modes with different  $m_p$ . In the top panel of Fig. 3c, we present optical spectra compiled from a single microring, where each colorband corresponds to a different  $m_p$  value - stepping  $m_p$  by one shifts  $\nu_s$  into a new colorband. Hence, the relatively small  $\nu_p$  tuning range ( $\approx 8 \text{ THz}$ ) enables coarse  $\nu_s$  tuning between  $\approx 490 \text{ THz}$  and  $\approx 560 \text{ THz}$ . This coarse tuning mechanism was reported in ref. <sup>31</sup> and arises from the  $\nu_p$ -dependent  $\Delta\nu$  spectrum. In the bottom panel, we chart the  $\nu_{s,i}$  values extracted from the optical spectra above, and we compare our measurements to simulations. We find that simulations accurately predict the  $\nu_{s,i}$  shifts that result from incrementing  $m_p$ . The  $\nu_p$  variation (for a given  $m_p$ ) that is evident in Fig. 3c is due to an underlying RW variation (i.e., moving along a line of constant  $m_p$  corresponds to varying RW). In Fig. 3c, bold data are associated with the first  $\mu\text{OPO}$  observed when  $\nu_p$  is scanned into resonance from blue to red detunings, and faded data are associated with subsequent  $\mu\text{OPO}$ s observed during the scan. We typically observe between six and eight  $\mu\text{OPO}$ s for each  $m_p$  value, as shown in Fig. 3b.

### Tunability and coherence

The spectra in Fig. 3c come from one device and exhibit spectral gaps in between colorbands. To address these gaps, we fabricate three more devices with small

systematic RW differences. Detailed data for these devices are shown in Supplementary Information Fig. S4. In Fig. 4a, we present optical spectra compiled from this set of four devices that address the entire green gap with nearly FSR-level resolution. In particular, we use just two devices to generate more than 100  $\mu\text{OPO}$ s, including all signal frequencies above 490 THz, and further design optimization could allow similar performance using only one device. For instance, using a larger RR will increase the density of longitudinal modes (and, in turn, the density of spectral coverage), employing chip-integrated heaters will allow thermo-optic dispersion control to actuate FSR-level  $\nu_s$  tuning<sup>44</sup>, and the (H, U) design could be further optimized. Still, understanding the intertwined roles of these various “knobs” is a work in progress. We also note that the highest frequency achieved in our study, as detailed in Supplementary Information Fig. S3, is  $\approx 563.51 \text{ THz}$ , which is nearly 15 THz beyond the previous record<sup>32</sup>. Moreover, since many applications (e.g., spectroscopy of quantum systems - see marked level transitions in Fig. 4a) require lasers that are continuously tunable and phase coherent, we proceed to characterize the  $\nu_s$  tunability and measure the  $\mu\text{OPO}$  linewidth. As described above, a useful coupling exists between  $\nu_p$  and  $\nu_s$ , where small adjustments to the former (e.g., shifting the pump-resonator detuning) can induce FSR-level shifts in the latter. It is also crucial to understand the tuning dynamics in between such mode hops. In Fig. 4b, we present measurements of  $\nu_s$ , recorded using an optical spectrum analyzer (OSA), as  $\nu_p$  is tuned in our nominal device. We observe that, in between mode hops, the tuning coefficient  $d\nu_s/d\nu_p \approx 1$  (it is slightly greater than one due to thermo-optic shifts); and typically, we achieve continuous tuning ranges between 50 GHz and 80 GHz. Notably, this tuning range depends on the dispersion and can be extended using, e.g., integrated temperature control<sup>44</sup>, and we show some preliminary experimental results with temperature variation in Supplementary Information Fig. S5. We note that ‘bumpiness’ in Fig. 4b (i.e., any deviation from linear tuning) is primarily due to OSA error.

Next, we record radiofrequency spectra from heterodyne beats between the  $\mu\text{OPO}$  signal and a low-noise tunable continuous-wave laser. Here, we use the full-width at half maximum (FWHM) of observed spectral lineshapes to approximate the  $\mu\text{OPO}$  signal linewidth. In particular, we are interested in relative orders of magnitude between the pump laser linewidth ( $\approx 300 \text{ kHz}$ ) and  $\mu\text{OPO}$  linewidths, and we reserve a more comprehensive noise analysis for future studies. In Fig. 4c, we present heterodyne spectra for three  $\mu\text{OPO}$ s with signal frequencies near 470 THz, 504 THz, and 523 THz. Respectively, the fitted lineshapes exhibit FWHM values of  $\approx 547 \text{ kHz}$ ,  $\approx 482 \text{ kHz}$ , and  $\approx 504 \text{ kHz}$ , where the figure



includes the one standard deviation uncertainties obtained from the fits. These values are commensurate with the pump laser linewidth and demonstrate low added noise from the  $\mu$ OPO; moreover, they are much smaller than typical III-V diode lasers in this wavelength range. In a more absolute sense, the measured linewidths are already sufficiently small for many high-coherence applications, and future systems could employ injection locking to achieve low-noise operation even with noisy pump lasers<sup>22,45,46</sup>.

## Discussion

In summary, we establish a blueprint, based on widely separated Kerr OPO, for integrated sources of coherent and highly tunable light at green-gap frequencies. We

generate the most widely separated  $\mu$ OPOs to date, with a signal frequency reaching  $\approx 563.51$  THz and its corresponding idler near  $\approx 207.28$  THz. Dispersion simulations suggest that cyan emission is possible with our scheme, but it is currently not observed due to parasitic losses in the idler band. Finally, we note that the resonator-waveguide coupling was not optimized to realize large conversion efficiencies, but we expect that conventional strategies to increase coupling (e.g., using pulley waveguide geometries<sup>30</sup>) will enable efficient green emission. Preliminary measurements, presented in Supplementary Information section V, indicate that engineered coupling waveguides can improve efficiency; in a pulley-coupled test device we estimate the on-chip signal power to be  $\approx 500 \mu\text{W}$  (Supplementary

Information Fig. S7), and higher power is possible after further coupling optimization<sup>30</sup>.

## Materials and methods

Simulations in Figs. 2 and 3 are based on eigenmode calculations of the microrings using the finite-element method. The layout of the devices is prepared using the Nanolithography Toolbox, a free software package provided by the NIST Center for Nanoscale Science and Technology<sup>47</sup>. A 605-nm-thick layer of SiN is deposited by low-pressure chemical vapor deposition on top of a 3  $\mu\text{m}$  SiO<sub>2</sub> layer on a 100 mm Si wafer. Spectroscopic ellipsometry is employed to measure the layer thicknesses and the wavelength-dependent refractive indices, and the results are fitted using an extended Sellmeier model. The device patterning is realized using positive-tone resist and electron-beam lithography, followed by pattern transfer into the SiN layer through reactive-ion etching using a CF<sub>4</sub>/CHF<sub>3</sub> chemistry. The device undergoes chemical cleaning to remove any residual polymer or resist post-etching and is subsequently annealed at 1100 °C in a nitrogen environment for four hours. An oxide lift-off process is executed to ensure air-cladding on the devices while maintaining oxide-cladding over the input and output waveguides. The chip is then diced and polished for lensed-fiber coupling. The microring undercut is achieved by heated KOH etching at 70 °C, with the lateral etching rate estimated by measuring the vertical etching rate and verified through cross-sectional scanning electron microscope images.

## Acknowledgements

This work is partially supported by the DARPA LUMOS and NIST-on-a-chip programs. X.L. acknowledges supports from Maryland Innovation Initiative. We thank Dr. Ashish Chanana for help with experiments.

## Author details

<sup>1</sup>Microsystems and Nanotechnology Division, Physical Measurement Laboratory, National Institute of Standards and Technology, Gaithersburg, MD, USA. <sup>2</sup>Joint Quantum Institute, NIST/University of Maryland, College Park, MD, USA. <sup>3</sup>Reality Labs Research, Meta, Redmond, WA, USA

## Author contributions

Xiyuan Lu, Yi Sun, and Jordan Stone carried out the device design and simulation. Xiyuan Lu, Yi Sun, and Junyeob Song carried out the fabrication. Yi Sun, Jordan Stone, Xiyuan Lu, and Feng Zhou carried out the measurements. All authors participated in analysis and discussion of results. Jordan Stone and Yi Sun wrote the manuscript with help from others, and Kartik Srinivasan supervised the project.

## Data availability

The data that supports the plots within this paper and other findings of this study are available from the corresponding author upon reasonable request.

## Conflict of interest

The authors declare no competing interests.

**Supplementary information** The online version contains supplementary material available at <https://doi.org/10.1038/s41377-024-01534-x>.

Received: 22 January 2024 Revised: 8 July 2024 Accepted: 15 July 2024  
Published online: 21 August 2024

## References

- Chellappan, K. V., Erden, E. & Urey, H. Laser-based displays: a review. *Appl. Opt.* **49**, F79–F98 (2010).
- Zhao, J. Y. et al. Full-color laser displays based on organic printed microlaser arrays. *Nat. Commun.* **10**, 870 (2019).
- Hummon, M. T. et al. Photonic chip for laser stabilization to an atomic vapor with 10<sup>-11</sup> instability. *Optica* **5**, 443–449 (2018).
- Shang, H. S. et al. Laser with 10<sup>-13</sup> short-term instability for compact optically pumped cesium beam atomic clock. *Opt. Express* **28**, 6868–6880 (2020).
- Zou, D. et al. Sensing earth rotation with a helium-neon laser operating on three transitions in the visible region. *Appl. Opt.* **58**, 7884–7891 (2019).
- Luke, A. M. et al. Lasers: a review with their applications in oral medicine. *J. Lasers Med. Sci.* **10**, 324–329 (2019).
- Moody, G. et al. Roadmap on integrated quantum photonics. *J. Phys.: Photon.* **4**, 012501 (2022).
- Uppu, R. et al. Quantum-dot-based deterministic photon-emitter interfaces for scalable photonic quantum technology. *Nat. Nanotechnol.* **16**, 1308–1317 (2021).
- Pleasant, S. Overcoming the ‘green gap’. *Nat. Photon.* **7**, 585 (2013).
- Moustakas, T. D. & Paiella, R. Optoelectronic device physics and technology of nitride semiconductors from the UV to the terahertz. *Rep. Prog. Phys.* **80**, 106501 (2017).
- Hamada, H. et al. AlGaInP strained multiple-quantum-well visible laser diodes ( $\lambda_L \leq 630$  nm band) with a multi-quantum barrier grown on misoriented substrates. *IEEE J. Quant. Electron.* **29**, 1844–1850 (1993).
- Kitatani, T. et al. A 1.3- $\mu\text{m}$  GaInNAs/GaAs single-quantum-well laser diode with a high characteristic temperature over 200 K. *Jpn. J. Appl. Phys.* **39**, L86 (2000).
- Sun, Y. et al. Room-temperature continuous-wave electrically injected InGaIn-based laser directly grown on Si. *Nat. Photon.* **10**, 595–599 (2016).
- Ra, Y. H. et al. An electrically pumped surface-emitting semiconductor green laser. *Sci. Adv.* **6**, eaav7523 (2020).
- Mei, Y. et al. Quantum dot vertical-cavity surface-emitting lasers covering the ‘green gap’. *Light Sci. Appl.* **6**, e16199 (2017).
- Li, P. P. et al. Demonstration of yellow (568 nm) stimulated emission from optically pumped InGaIn/GaN multi-quantum wells. *Appl. Phys. Lett.* **121**, 071103 (2022).
- Corato-Zanarella, M. et al. Widely tunable and narrow-linewidth chip-scale lasers from near-ultraviolet to near-infrared wavelengths. *Nat. Photon.* **17**, 157–164 (2023).
- Sperling, J. et al. Breakthrough instruments and products: laser light tunable across the visible up to mid-infrared: novel turnkey cw OPO with efficiency-optimized design. *Rev. Sci. Instrum.* **92**, 129502 (2021).
- Schäfer, F. P. *Dye Lasers*. 1st edn (Springer Berlin, 1973).
- Wang, Y. B. et al. Photonic-circuit-integrated titanium:sapphire laser. *Nat. Photon.* **17**, 338–345 (2023).
- Carmon, T. & Vahala, K. J. Visible continuous emission from a silica microphotonic device by third-harmonic generation. *Nat. Phys.* **3**, 430–435 (2007).
- Ling, J. W. et al. Self-injection locked frequency conversion laser. *Laser Photon. Rev.* **17**, 2200663 (2023).
- Guo, X., Zou, C.-L. & Tang, H. X. Second-harmonic generation in aluminum nitride microrings with 2500%/W conversion efficiency. *Optica* **3**, 1126–1131 (2016).
- Surya, J. B. et al. Efficient third-harmonic generation in composite aluminum nitride/silicon nitride microrings. *Optica* **5**, 103–108 (2018).
- Levy, J. S. et al. Harmonic generation in silicon nitride ring resonators. *Opt. Express* **19**, 11415–11421 (2011).
- Lu, X. Y. et al. Efficient photoinduced second-harmonic generation in silicon nitride photonics. *Nat. Photon.* **15**, 131–136 (2021).
- Nitiss, E. et al. Optically reconfigurable quasi-phase-matching in silicon nitride microresonators. *Nat. Photon.* **16**, 134–141 (2022).
- Sayson, N. L. B. et al. Octave-spanning tunable parametric oscillation in crystalline Kerr microresonators. *Nat. Photon.* **13**, 701–706 (2019).
- Lu, X. Y. et al. Milliwatt-threshold visible-telecom optical parametric oscillation using silicon nanophotonics. *Optica* **6**, 1535–1541 (2019).
- Stone, J. R. et al. Efficient chip-based optical parametric oscillators from 590 to 1150 nm. *APL Photon.* **7**, 121301 (2022).



31. Lu, X. Y. et al. On-chip optical parametric oscillation into the visible: generating red, orange, yellow, and green from a near-infrared pump. *Optica* **7**, 1417–1425 (2020).
32. Domenegueti, R. R. et al. Parametric sideband generation in CMOS-compatible oscillators from visible to telecom wavelengths. *Optica* **8**, 316–322 (2021).
33. Lu, X. Y. et al. Kerr optical parametric oscillation in a photonic crystal microring for accessing the infrared. *Opt. Lett.* **47**, 3331–3334 (2022).
34. Tang, Y. L. et al. Widely separated optical Kerr parametric oscillation in AlN microrings. *Opt. Lett.* **45**, 1124–1127 (2020).
35. Pidgayko, D. et al. Voltage-tunable optical parametric oscillator with an alternating dispersion dimer integrated on a chip. *Optica* **10**, 1582–1586 (2023).
36. Black, J. A. et al. Optical-parametric oscillation in photonic-crystal ring resonators. *Optica* **9**, 1183–1189 (2022).
37. Perez, E. F. et al. High-performance Kerr microresonator optical parametric oscillator on a silicon chip. *Nat. Commun.* **14**, 242 (2023).
38. Ledezma, L. et al. Octave-spanning tunable infrared parametric oscillators in nanophotonics. *Sci. Adv.* **9**, eadf9711 (2023).
39. Lu, J. J. et al. Ultralow-threshold thin-film lithium niobate optical parametric oscillator. *Optica* **8**, 539–544 (2021).
40. Bruch, A. W. et al. On-chip  $\chi^{(2)}$  microring optical parametric oscillator. *Optica* **6**, 1361–1366 (2019).
41. Stone, J. R. et al. Conversion efficiency in Kerr-microresonator optical parametric oscillators: from three modes to many modes. *Phys. Rev. Appl.* **17**, 024038 (2022).
42. Isichenko, A. et al. Chip-scale, sub-Hz fundamental sub-kHz integral linewidth 780 nm laser through self-injection-locking a Fabry-Pérot laser to an ultra-high Q integrated resonator. *arXiv* <https://doi.org/10.48550/arXiv.2307.04947> (2023).
43. Zhang, Z. Y. et al. Photonic integration platform for rubidium sensors and beyond. *Optica* **10**, 752–753 (2023).
44. Moille, G. et al. Integrated buried heaters for efficient spectral control of air-clad microresonator frequency combs. *APL Photon.* **7**, 126104 (2022).
45. Li, B. H. et al. High-coherence hybrid-integrated 780 nm source by self-injection-locked second-harmonic generation in a high-Q silicon-nitride resonator. *Optica* **10**, 1241–1244 (2023).
46. Clementi, M. et al. A chip-scale second-harmonic source via self-injection-locked all-optical poling. *Light Sci. Appl.* **12**, 296 (2023).
47. Balram, K. C. et al. The nanolithography toolbox. *J. Res. Natl Inst. Stand. Technol.* **121**, 464–475 (2016).